

Electro-Absorption Modulation in GeSn Alloys for Wide-Spectrum Mid-Infrared Applications

Yun-Da Hsieh

National Chung Cheng University

Jun-Han Lin

National Chung Cheng University

Richard Soref

University of Massachusetts

Greg Sun

Department of Engineering, University of Massachusetts Boston

Hung-Hsiang Cheng

National Taiwan University

Guo-En Chang (✉ imegec@ccu.edu.tw)

National Chung Cheng University <https://orcid.org/0000-0002-3739-5451>

Article

Keywords: EPICs, CMOS, MIR, FK

Posted Date: January 12th, 2021

DOI: <https://doi.org/10.21203/rs.3.rs-138946/v1>

License:  This work is licensed under a Creative Commons Attribution 4.0 International License.

[Read Full License](#)

Version of Record: A version of this preprint was published at Communications Materials on April 9th, 2021. See the published version at <https://doi.org/10.1038/s43246-021-00144-z>.

Electro-absorption modulation in GeSn alloys for wide-spectrum mid-infrared applications

Yun-Da Hsieh,¹ Jun-Han Lin,¹ Richard A. Soref,² Greg Sun,² H. H. Cheng,³
and Guo-En Chang^{1,*}

¹Department of Mechanical Engineering and Advanced Institute of Manufacturing with High-tech Innovations, National Chung Cheng University, Chiayi County 62102, Taiwan

²Department of Engineering, University of Massachusetts–Boston, Boston, Massachusetts 02125, United States

³Center for Condensed Matter Sciences and Graduate Institute of Electronics Engineering, National Taiwan University, Taipei 10617, Taiwan

*correspondence and material requests should be addressed to G. E. Chang. (email:imegec@ccu.edu.tw)

Abstract

Si-based electronic-photonic integrated circuits (EPICs), which are compatible with state-of-the-art complementary metal-oxide-semiconductor (CMOS) processes, offer promising opportunities for on-chip mid-infrared (MIR) photonic systems. However, the lack of efficient MIR optical modulators on Si hinders the utilization of MIR EPICs. Here, we clearly demonstrate the Franz-Keldysh (FK) effect in GeSn alloys and achieve on-Si MIR electro-absorption optical modulation using GeSn heterostructures. Our experimental and theoretical results verify that the direct bandgap energy of GeSn can be widely tuned by varying the Sn content, thereby realizing wavelength-tunable optical modulation in the MIR range with a figure-of-merit of $\Delta\alpha / \alpha_0$ (FOM) greater than 1.5 and a broadband operating range greater than 140 nm. In contrast to conventional silicon-photonic modulators based on the plasma dispersion effect, our GeSn heterostructure demonstrates practical and effective FK MIR optical modulation on Si and helps unlock the potential of MIR EPICs for a wide range of applications.

Introduction

The tremendous success of Si electronics has driven research and development on Si-based electronic-photonic integrated circuits (EPICs), the so-called “superchips” combining photonic applications with electronics that can be seamlessly fabricated in a complementary metal-oxide-semiconductor (CMOS)-compatible processes¹. Si-based EPICs prepared using group-IV semiconductors including Si, Ge, and their alloys, have achieved unprecedented success in the near-infrared (NIR) region spanning from 0.7 μm to 1.4 μm ³⁻⁵. The operating wavelength of Si-based EPICs is currently being expanded to the mid-infrared (MIR) spectral region (typically defined as the 1.8–5 μm wavelength range⁶) for a broad range of applications such as high-speed optical communications, bio-medical sensing, environmental monitoring, astronomy, and long-range lidar detection⁶⁻⁹. MIR EPICs require the monolithic integration of light sources, waveguides, amplifiers, modulators, switches, and photodetectors on a single Si substrate. Although significant progress has been made on MIR Si-based waveguides¹⁰, light emitters¹¹⁻¹⁶, and photodetectors¹⁷⁻²⁰, efficient MIR optical modulators on Si remain elusive because group-IV semiconductors do not exhibit the linear electro-optical (Pockels) effect²¹.

The electric field effect is the ideal control mechanism for optical modulation because it requires little or no electric current (and therefore little power) and delivers fast response suitable for >100 GHz high-speed modulation^{22,23}. An applied electric field can induce a change in either the real (Δn) or the imaginary part of the refractive index ($\Delta\alpha$) of some materials, known as electro-refraction or electro-absorption (EA), respectively. The Franz–Keldysh (FK) effect is an EA phenomenon in which the modulation wavelength is determined by the direct-gap absorption edge of the material. Although the FK effect in GeSn alloys can be effective for implementing on-chip MIR optical modulation²⁴ and the FK effect in GeSn alloys has been observed²⁵, MIR modulation has not yet been experimentally realized.

In this paper, we present a series of experimental results on the achievement of EA modulation on Si using GeSn alloys offering high-performance in the 1.95–2.25 μm MIR wavelength range, which can be extended readily to 5 μm in modified versions. The GeSn alloy used here is part of the group-IV photonics (GFP) approach, an expanded version of silicon photonics employing SiGeSn materials. The device is comprised of a small circular mesa that

has free-space light incident normally upon it. A reverse-biased *p-i-n* diode structure modulates the intensity of light transmitted through the Si substrate. This device is a *p-Ge/i-GeSn/n-Ge* heterostructure diode grown upon Ge-buffered Si substrates and is a CMOS-compatible device that utilizes the FK effect to shift the zero-field absorption spectrum of the GeSn active region. The detailed measurements presented here, which are confirmed by our theoretical modeling, demonstrate that GeSn alloys can be efficient MIR optical modulators on Si. We show that control of the Sn content in the GeSn active layer provides a broadband operating range of >140 nm and a good figure-of-merit (FOM) of $\Delta\alpha/\alpha_0 \sim 1.5$ across the MIR range. We also theoretically study the effect of Sn content and strain on the FK effect in GeSn. These results experimentally demonstrate a practical approach for achieving MIR optical modulation on Si using GeSn alloys and open up new avenues for Si-based MIR EPICs.

There are fundamental-physics reasons why the present approach is quite competitive with alternative GFP modulation schemes. Unlike Ge which has an indirect bandgap, GeSn alloys have nearly direct or direct bandgap which can be easily tuned by varying the alloy composition. While excellent Ge-based EA modulators have been reported^{23,26,27}, the 0.8 eV direct bandgap in Ge limits its operating wavelength to only approximately 1600 nm. The quantum-confined Stark effect (QCSE) in Ge quantum wells^{28,29} has a similar limitation. If we examine the free-carrier plasma dispersion effect in GeSn and Ge as a competing EA modulation mechanism³⁰⁻³², the free-carrier approach is weaker because it requires a larger interaction length than the FK effect and usually consumes a significant amount of power up to hundreds of milliwatts.

Results

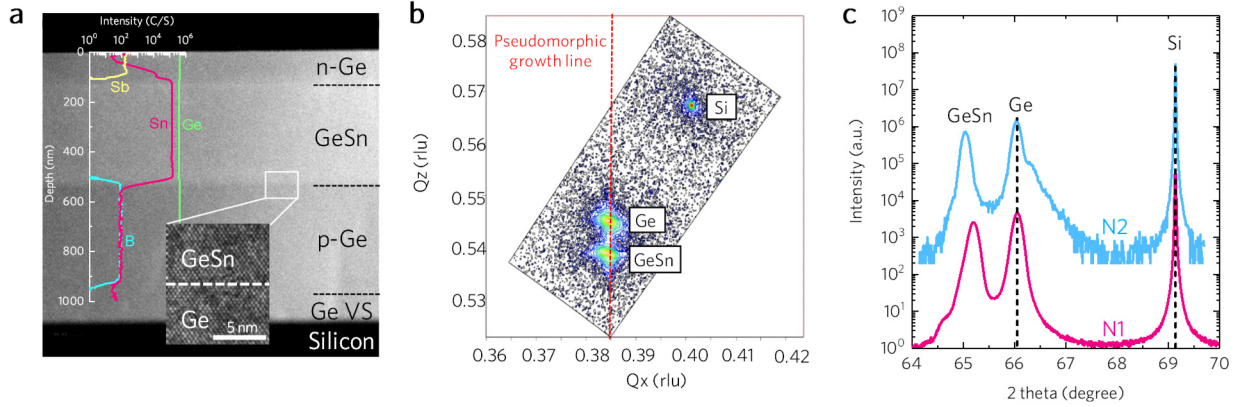


Figure 1. Material characterization of the grown samples. (a) Cross-sectional transmission electron microscopy (XTEM) image of sample N1 overlapped with secondary ion mass spectrometry (SIMS) atomic distribution. The inset shows a high-resolution XTEM image of the Ge/GeSn interface, revealing pseudomorphic growth. (b) (224) reciprocal-space mapping (RSM) of sample N1, showing pseudomorphic GeSn/Ge heterostructures. (c) ω - 2θ scan of the samples, showing shifted GeSn peaks with increasing Sn composition.

Material growth and characterization

In this study, we investigated GeSn double-barrier heterostructures (DHB) with different Sn contents for MIR EA modulation. The heterostructure consists of a pseudomorphic *p-i-n* Ge/GeSn/Ge diode structures grown on a double-side polished (001) silicon substrate via a Ge virtual substrate (VS) using low-temperature molecular beam epitaxy (MBE) (see the Methods section). To study the effect of Sn content on the FK effect in GeSn, two samples (N1, N2) were epitaxially grown with N2 having a higher Sn content than N1. Figure 1(a) shows a cross-sectional transmission electron microscopy (XTEM) image of sample N1 overlapped with secondary ion mass spectrometry (SIMS) atomic distribution profiles of Ge, Sn, B, and Sb. From the XTEM image, defects were observed to be confined at the interface near the Si substrate, indicating the strain relaxation of Ge VS. Clear, flat, and sharp interfaces between the Ge and GeSn layers were observed, indicating a good quality Ge/GeSn/Ge heterostructure. An average threading dislocation density (TDD) of $3.9 \times 10^{-7} \text{ cm}^{-2}$ was obtained for the grown samples via

etch-pit density experiments, which is comparable with the typical value of $\sim 2 \times 10^7 \text{ cm}^{-2}$ in good quality Ge-on-Si materials³³. In addition, the SIMS results reveal a homogenous distribution of Sn atoms in the GeSn layer. X-ray diffraction (XRD) was employed to measure the lattice constants of the layers to determine Sn composition and strain. The (224) reciprocal space mapping (RSM) of sample N1 is displayed in Fig. 1(b). Three distinct peaks associated with the Si substrate, Ge layers, and GeSn active layer are observed. The Ge and GeSn peaks share the same Q_x , confirming that the GeSn layer is fully strained to the underlying Ge VS, which is consistent with the XTEM results. Fig. 1(c) shows high-resolution XRD ω - 2θ scans of the samples. The out-of-plane and in-plane lattice constants of the layers are determined using the Bragg angle (θ) and the pseudomorphic growth condition; the Sn composition and strain are then extracted using these results (Supplementary Note 1). The characterization results for the epitaxially grown samples are summarized in Table 1. Additionally, although the GeSn active layers were unintentionally doped, defects as vacancies or dislocations may introduce a p -type background carrier concentration. To obtain the background carrier concentration, a reference sample containing a 400-nm-thick $\text{Ge}_{0.955}\text{Sn}_{0.045}$ layer was grown on a Si substrate via a Ge VS under the same growth conditions, and Hall measurements showed a p -type background carrier concentration of $6.47 \times 10^{16} \text{ cm}^{-3}$.

Table 1. Characterization results obtained for the epitaxially grown samples

Sample	Sn %	GeSn layer thickness t (nm)	In-plane strain ϵ^{\parallel}
N1	4.82	420	-0.60%
N2	5.76	360	-0.74%

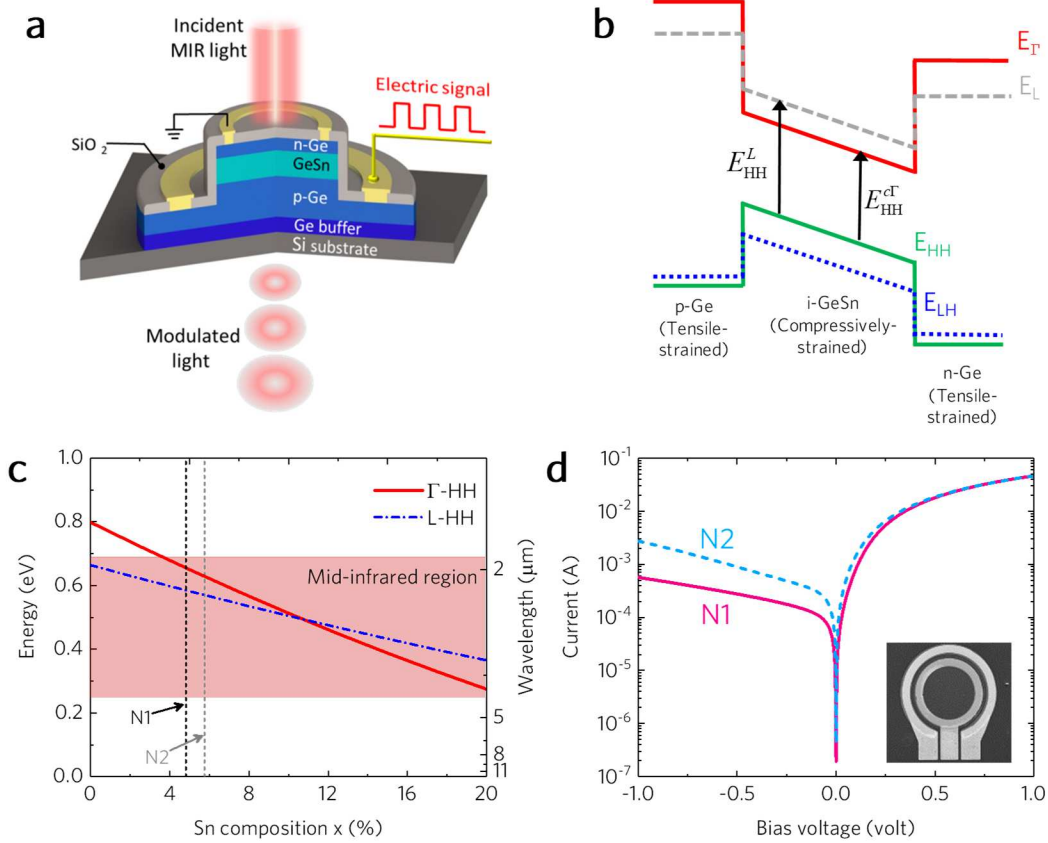


Figure 2. GeSn *p-i-n* diodes on silicon for MIR EA modulation. (a) Schematic of our designed normal-incident GeSn *p-i-n* diode on (001) silicon for optical modulation (not to scale). The mid-infrared (MIR) light beam is incident on the top of the device and transmitted through the GeSn active layer. AC bias voltage is applied to the *p-i-n* diode to modulate the MIR light based on the FK effect. (b) Schematic band diagram of Ge/GeSn/Ge heterojunction with an applied electric field. The compressive strain in the GeSn active layer splits the valence band. (c) Evolution of the lowest direct-gap transition energy (from the heavy-hole (HH) to Γ -conduction band) and indirect-gap transition energy (HH to L-conduction band) for pseudomorphic GeSn on Ge at 300 K as a function of Sn composition calculated using deformation potential theory. The epitaxially grown GeSn heterostructure samples N1 and N2 are indicated by the dashed lines. (d) Current-voltage characteristics of the fabricated GeSn *p-i-n* diodes with $D=250 \mu\text{m}$. The inset shows top-view scanning electron microscopy (SEM) image of the fabricated diode.

Device design and MIR modulation principle

Figure 2(a) shows a schematic diagram of the designed surface-illuminated GeSn *p-i-n* diode for optical modulation. The device consists of a pseudomorphic *p-Ge/i-GeSn/n-Ge* heterostructure grown on a silicon substrate via a Ge virtual substrate (VS) in which the narrow-bandgap GeSn layer is employed as an active layer. The application of a reverse bias to the device increases the electric field in the GeSn active layer, triggering the FK effect to modify the absorption coefficient near the direct-gap absorption edge of the GeSn active layer. Therefore, when light is normally incident on the surface of the device, the intensity of the transmitted light can be altered to achieve optical modulation. Figure 2(b) shows a schematic band diagram of the Ge/GeSn/Ge *p-i-n* heterostructure. Because the GeSn active layer has a smaller bandgap than that of Ge, a type-I band alignment at the Γ symmetry point in the momentum space can be achieved. In addition, the pseudomorphic growth of GeSn on Ge VS imposes a compressive strain in the GeSn active layer, thereby removing the degeneracy of heavy-hole (HH) and light-hole (LH) bands such that the top valence band is HH-like. As a result, the lowest direct-gap transition is from the HH band to the Γ -conduction band (HH \rightarrow c Γ), and the lowest indirect-gap transition is from the HH band to the L-conduction band (HH \rightarrow L). Note that the bandgap energies of the GeSn active layer can be widely tuned by controlling the Sn content. Thus, the modulation range of GeSn is expected to be "tunable" in the MIR region enabling a wide range of applications. In this study, we investigated the FK effect and optical modulation characterization in the GeSn devices with different Sn contents (devices N1 and N2). Figure 2(c) shows the lowest direct and indirect bandgap energies at $T=300$ K as a function of Sn composition of the GeSn active layer, which is obtained from our *k*·*p* calculations (Supplementary Note 5). As the Sn content increases, both direct and indirect bandgap energies decrease. With a Sn content of more than 3.6%, the direct bandgap can be reduced to <0.688 eV, thereby pushing the modulation range into the MIR region. In addition, a further increase in the Sn content allows bandgap shrinking and redshifting of the modulation range across the MIR region.

The device fabricated in this study is composed of a GeSn heterostructure *p-i-n* diode arranged vertically through two circular mesas of different diameters (D) and two ring-shaped Cr/Au metal pads. The device was fabricated using a standard CMOS-compatible process (see Methods

section). A scanning electron microscopy (SEM) image of the fabricated device with $D = 250 \mu\text{m}$ is displayed inset of Fig. 2(d). Figure 2(d) shows the current-voltage characteristics of the fabricated GeSn p - i - n diodes; clear rectifying behavior was observed. In addition, device N2 exhibited higher dark current than that of the device N1 under reverse bias conditions. The higher Sn content of device N2 resulted in a lower GeSn active layer bandgap¹⁵.

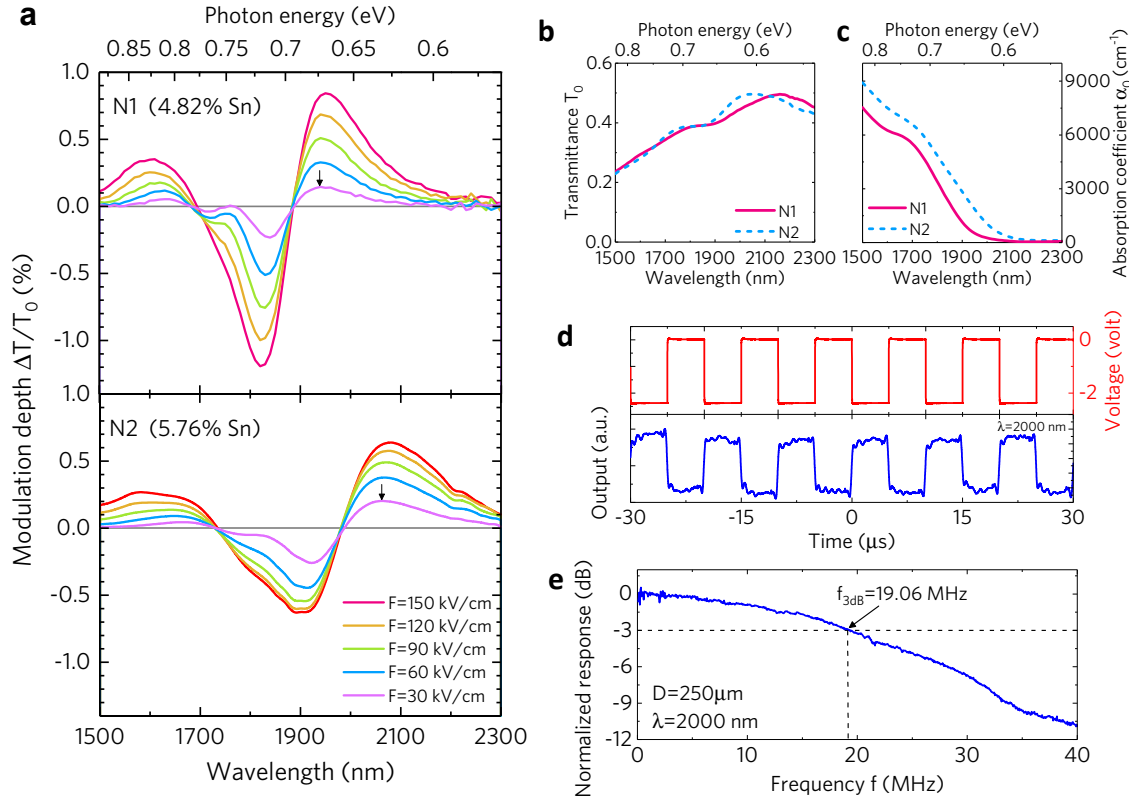


Figure 3. Modulation characteristics at room temperature: (a) Modulation depth spectra of the GeSn devices measured at different applied electric fields. Clear variations in transmittance are observed, providing strong evidence of the FK effect. The lowest direct transition energies are indicated by the solid arrows. (b) Transmittance spectra for the GeSn devices and (c) absorption spectra under zero bias conditions for the GeSn active layers. (d) AC optical modulation at 100 kHz at 2000 nm wavelength for device N1. (e) Normalized radio frequency response of device N1 ($D=250 \mu\text{m}$) at 2000 nm showing a 3 dB bandwidth of 19.06 MHz.

Experimental evidence of electro-absorption modulation in the mid-infrared region

The EA modulation properties of the GeSn devices are presented in Fig. 3. Figure 3(a) shows the measured modulation depth (MD) of the devices. MD is defined as $\Delta T(F)/T_0 = [T_0 - T(F)]/T_0$ ³⁴, where T_0 and $T(F)$ are the transmittance of the devices measured at zero bias (corresponding to a built-in electric field of $F_0=6$ kV/cm estimated using the depletion theory²²) and at different electric fields (F), respectively. The zero-bias transmittance spectra and absorption coefficient (α_0) spectra obtained from responsivity characterization (Supplementary Note 2) are presented in Figs. 3(b) and (c), respectively. At $F=30$ kV/cm, the MD spectra clearly show significant oscillation characteristics in the 1500–2300 nm spectral range in which the positive peaks (indicated by the arrows) are associated with the HH \rightarrow c Γ direct-gap transitions, which match the absorption edges in Fig. 3(c). The HH \rightarrow c Γ transition energies were determined to be $E_{\text{HH}}^{\text{c}\Gamma} = 0.639$ eV for device N1 and $E_{\text{HH}}^{\text{c}\Gamma} = 0.605$ eV for device N2. These results confirmed the narrowing of direct bandgap energies due to Sn-alloying. As the electric field increases, the MD significantly increases. With $F=150$ kV/cm, the MDs are 0.84% (87.1 dB/mm) at $\lambda=1950$ nm for device N1 and 0.64 % (77.4 dB/mm) at $\lambda=2080$ nm for device N2. In addition, the MD spectra exhibit redshift as the electric field increases because of the electric-field-induced tilting of the energy bands. These observations provide strong evidence for the FK effect in GeSn alloys. Figure 3(d) shows the AC modulation signal at $\lambda=2000$ nm for device N1 at 100 kHz and clear dynamical modulation is observed. These results exhibit optical modulation in the MIR region with the GeSn heterostructure devices. Figure 3(e) shows the normalized RF frequency response at 2000 nm of device N1. A 3 dB bandwidth ($f_{3\text{dB}}$) of 19.06 MHz was obtained, which is sufficient for many MIR applications such as Lidar, remote-sensing, and imaging^{6,9}. As the bandwidth of EAMs is limited by RC time delay²², it is anticipated that the modulation bandwidth can be increased by further reducing the device footprint (Supplementary Note 4).

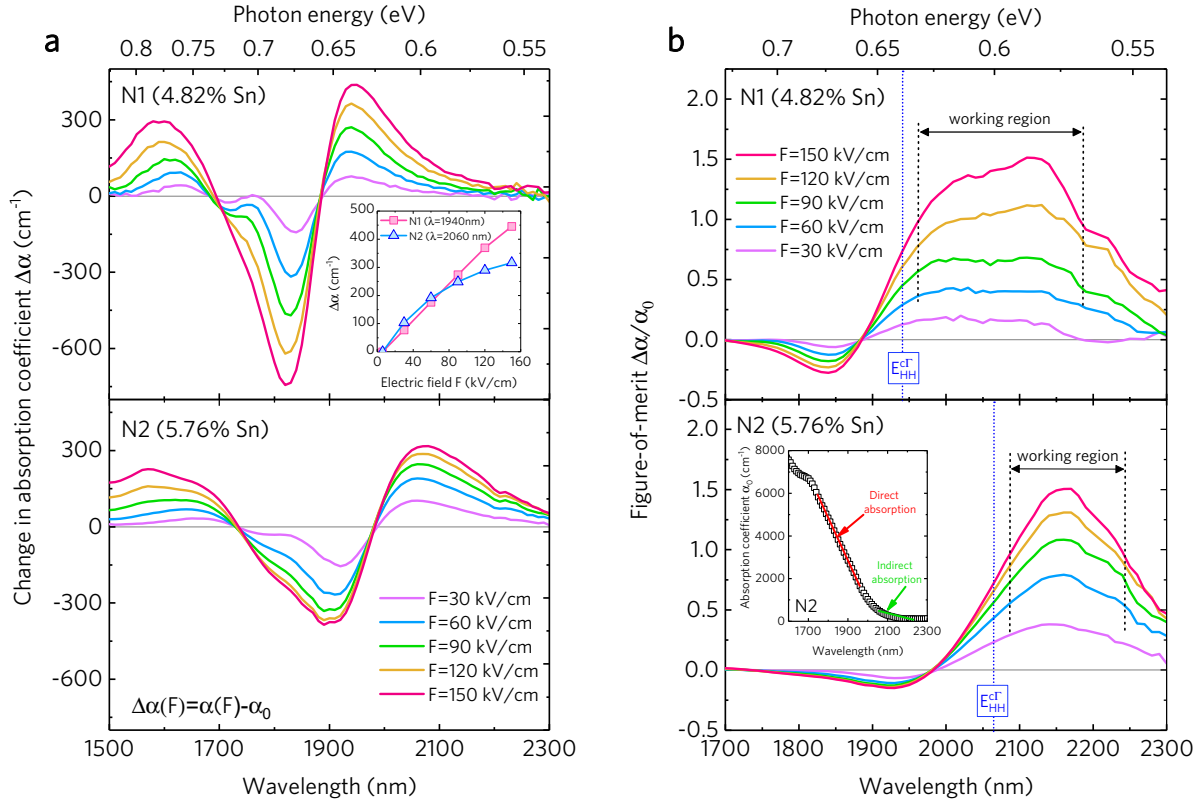


Figure 4. Franz-Keldysh effect in GeSn. (a) Change in the absorption coefficient in the GeSn active layers at different applied electric fields. The inset shows the change in the absorption coefficient for device N1 and device N2 at $\lambda=1940$ and $\lambda=2060$ nm, respectively, as a function of electric field. (b) Figure-of-merit (FOM) $\Delta\alpha/\alpha_0$ for the GeSn active layer at different applied electric fields. The lowest direct bandgap is indicated by the dashed blue lines. The inset shows the absorption coefficient spectrum under the zero-bias condition of device N2.

Electro-absorption Franz-Keldysh effect in GeSn

To further analyze the FK effect, the change in absorption coefficient ($\Delta\alpha$) with different electric fields for the GeSn active layer was extracted from the MD spectra using $\Delta\alpha = -\frac{1}{t} \ln[1 + \Delta T(F)/T_0]$, and the results are shown in Fig. 4(a). The $\Delta\alpha$ spectra clearly exhibit characteristic oscillation features that are very similar to the FK effects in III-V direct-bandgap materials²². The observed positive $\Delta\alpha$ peaks are located near $\lambda=1940$ nm for device N1 and $\lambda=2060$ nm for device N2, and the effect of the electric field on $\Delta\alpha$ is shown inset of Fig. 4(a). The absorption coefficient increases with increasing electric field but tends to saturate in high electric fields. For the electric field range of 6–50 kV/cm, we obtain $\Delta\alpha / \Delta F \sim 3.1 \text{ cm}^{-1}\text{kV}^{-1}$ for the devices, which is close to $\Delta\alpha / \Delta F \sim 3 \text{ cm}^{-1}\text{kV}^{-1}$ at $\lambda=1647$ nm in the 14–70 kV/cm range for Ge³⁵. At $F=150$ kV/cm, significant changes in the absorption coefficient of 437 cm^{-1} at $\lambda=1940$ nm for device N1 and 316 cm^{-1} at $\lambda=2060$ nm for device N2 were achieved. It is noted that the obtained $\Delta\alpha$ values decreases as the Sn content increases. This observation is attributed to the compressive strain in the GeSn layer, which will be discussed later.

While a high extinction ratio is favorable for optical modulators, a low insertion loss is equally essential. Thus, the FOM, defined as $\Delta\alpha / \alpha_0$, is usually used for characterizing materials for EA modulators and for determining the optimal spectral working region. Figure 4(b) shows the FOM spectra for the devices with different applied electric fields. The FOM increases with increasing wavelength and reaches a maximum at a photon energy ~ 25 meV below the lowest direct bandgap ($E_{\text{HH}}^{\text{cf}}$) as indicated by the dashed blue lines. It then decreases again as the wavelength increases further. As the applied electric field increases, the FOM increases with an increase in $\Delta\alpha$. At $F=150$ kV/cm, the FOM peaks at 1.51 at $\lambda=2110$ nm for device N1 and 1.50 at $\lambda=2160$ nm for device N2. These values are comparable and slightly better than those of Ge-based EA modulators^{27,29}. This behavior can be explained by the contribution of the indirect transition to the background absorption coefficient. In pure Ge, the L-conduction band lies below the Γ -conduction band by a significant energy separation of $E_{\text{TL}} = 136$ meV. As a result, there is usually a long indirect absorption tail extending below the direct transition band edge, which contributes to a permanent high absorption coefficient below the direct-gap absorption edge

$(\alpha_L \propto (\hbar\omega - E_g^L \pm E_{\text{ap}})^2)$, where E_g^L is the indirect bandgap and E_{ap} is the acoustic phonon energy³⁶). Consequently, Ge-based EA modulators usually suffer from relatively high insertion losses and thus, low FOMs. In contrast, the energy difference $\Delta E_{\Gamma L}$ between the direct and indirect conduction bands in the GeSn devices is considerably reduced to 70 meV for device N1 and 58 meV for device N2. This significantly reduces α_L below the direct-gap absorption edge, as shown in the inset of Fig. 4(b). As a result, the FOM is enhanced, suggesting the potential for low insertion-loss and high extinction-ratio MIR optical modulation. We can also define the optimal modulation range of the devices based on the FOM. For device N1 (4.82% Sn), as shown in Fig. 4(b), the FOM at $F = 150$ kV/cm is always >1 across a wavelength range of 1964–2190 nm. This implies that the extinction ratio can indeed be greater than the insertion loss, which is beneficial for achieving high-performance optical modulation. Thus, we identify this 226-nm-wide spectral range as the operating regime of this device. For device N2 with a higher Sn content (5.76% Sn), the adequate modulation range is from 2090 nm to 2236 nm with a 146-nm-wide optimal modulation width. The corresponding scaling performance for device N1 (N2) is 66.32 dB/mm (95.9 dB/mm) extinction ratio and 49.8 dB/mm (64.7 dB/mm) insertion loss at $\lambda=2070$ nm ($\lambda=2160$ nm) (Supplementary Note 3). These results emphasize several unique advantages of MIR GeSn optical modulators. First, the adequate modulation range of these devices with a $\text{FOM} > 1$ is much larger than the modulation width of ~ 20 nm for Ge(Si) EA modulators²³ and free-carrier Si Mach-Zender optical modulators³⁷. This highlights the broadband optical modulation capability of GeSn in the MIR range. Second, the optimal modulation range of the GeSn devices can be controlled by varying the Sn composition in the GeSn active layer to achieve optical modulation at other spectral ranges in the MIR region. Third, the optimal modulation range of our devices perfectly matches the emerging 2 μm MIR optical communication band ($\lambda=1900\text{--}2100$ nm)^{6,31} and 2 μm ultra-long range Lidar⁹, making our devices ideal for MIR optical communication applications.

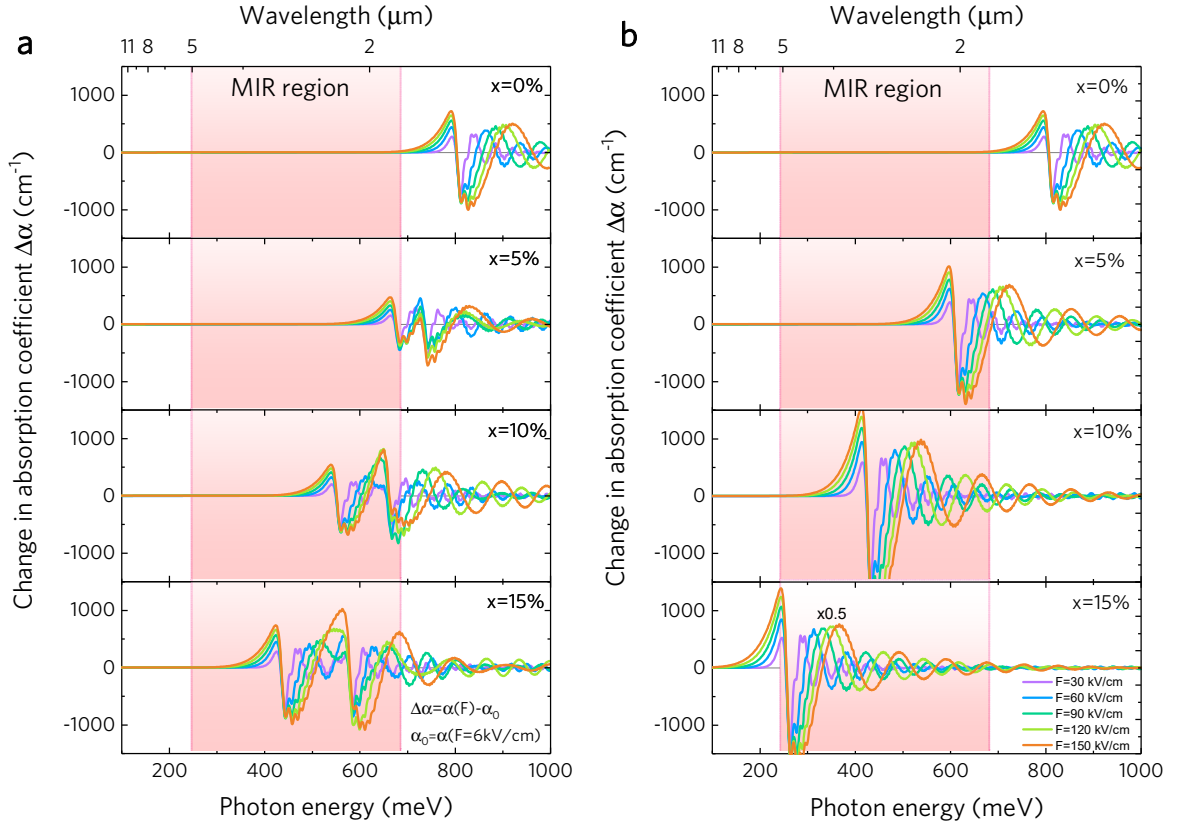


Figure 5. Theoretical modeling for Franz-Keldysh effect in GeSn. Calculated change-in-absorption coefficient $\Delta\alpha$ at $T=300$ K for (a) pseudomorphic $\text{Ge}_{1-x}\text{Sn}_x$ on Ge and (b) unstrained $\text{Ge}_{1-x}\text{Sn}_x$ with different Sn contents and electric fields.

Theoretical modeling of the Franz-Keldysh effect in GeSn

After the experimental verification of the FK effect and MIR EA modulation in GeSn, understanding the effect of GeSn alloy composition on the FK effect is essential for the design of efficient GeSn MIR EA modulators for MIR EPICs. Here, we discuss the effect of Sn composition up to 15% on the FK effect in GeSn. In addition, we also investigate the strain effect by comparing the electric-field-induced $\Delta\alpha$ for pseudomorphic $\text{Ge}_{1-x}\text{Sn}_x$ on Ge and unstrained $\text{Ge}_{1-x}\text{Sn}_x$. The theoretical models for strained band structures and electric-field-independent absorption coefficients are presented in Supplementary Notes 5 and 6^{22,38,39}. Fig. 5(a) shows the calculated $\Delta\alpha$ spectra for pseudomorphic $\text{Ge}_{1-x}\text{Sn}_x$ on Ge (which has a compressive

strain of 0.143% per one percent Sn) with different Sn compositions and electric fields. For a fixed Sn content, $\Delta\alpha$ increases with an increase in the electric field due to the FK effect. As the Sn content of the GeSn alloy increases, the direct bandgap decreases despite the compressive strain, redshifting the $\Delta\alpha$ spectrum. For $x>3.6\%$, the direct bandgap can be reduced to <0.688 eV, shifting the modulation range into the MIR region. For $x=15\%$, the modulation range can be shifted to ~ 3.1 μm . In addition, the magnitude of $\Delta\alpha$ near the direct bandgap edge is significantly dependent on the Sn content. When the Sn content increases from 0% to 5%, the magnitude of $\Delta\alpha$ near the direct bandgap edge decreases. This behavior is attributed to the compressive strain that splits the HH and LH bands. Thus, $\Delta\alpha$ arising from HH \rightarrow c Γ and LH \rightarrow c Γ transitions occurs at different photon energies. As a result, $\Delta\alpha$ near the direct bandgap edge is only governed by the HH \rightarrow c Γ transition, leading to a weaker FK effect (Supplementary Notes 6). This analysis matches our experimental observation (Fig. 4a). As the Sn content increases further from 5% to 15%, $\Delta\alpha$ near the direct bandgap edge again increases. This behavior is attributed to the increased joint density-of-states caused by the larger effective masses of electrons and holes that significantly enhance the direct-gap absorption coefficient (Supplementary Notes 6), thereby enhancing $\Delta\alpha$. In contrast, for unstrained Ge $_{1-x}$ Sn $_x$, the $\Delta\alpha$ spectrum also redshifts with an increase in the Sn content, but with a higher rate compared to the case of pseudomorphic Ge $_{1-x}$ Sn $_x$ on Ge. Thus, the modulation range can be widely tuned across the entire MIR region by varying the Sn content in the 2.8%–15% range. In addition, the HH and LH bands are still degenerate in the unstrained Ge $_{1-x}$ Sn $_x$ alloys. Thus, both HH \rightarrow c Γ and LH \rightarrow c Γ transitions can contribute to $\Delta\alpha$ near the direct bandgap, leading to a larger $\Delta\alpha$ compared to pseudomorphic Ge $_{1-x}$ Sn $_x$ on Ge. In addition, $\Delta\alpha$ monotonically increases with an increase in the Sn content. This highlights the importance of the strain effect on FK modulation in GeSn. The results of these GeSn strain and alloy composition experiments provide useful guidelines for designing high-performance GeSn MIR EA modulators.

Discussion.

We have presented the first experimental demonstration of MIR EA modulation using GeSn alloys on Si. The FK effect in the MIR region was clearly observed by engineering the bandgap of GeSn alloys with Sn-alloying. EA modulation in the MIR region was achieved with a good FOM of > 1.5 and a broadband modulation spectral range of >140 nm. In addition, our experimental and theoretical analyses verified that the modulation range can be tuned by adjusting the Sn composition to enable efficient optical modulation in the entire MIR spectrum. Room-temperature GFP EPICs can be utilized for a broad range of applications such as high-speed optical communications, remote sensing, environmental monitoring, astronomy, infrared imaging, and long-range Lidar detection over the entire MIR range, but more particularly in the new 2- μm communications band⁶. Another advantage of our GeSn heterostructure MIR device is its low-cost manufacturability and scalability using CMOS-compatible fabrication processes.

For the GeSn devices fabricated in this study, the mesa can be thought of as one pixel in an $N \times M$ -pixel spatial light modulator. But, moving away from the space scenario, it is a straightforward procedure to modify the heterostructure presented here to create an effective EA modulator within a strip-channel waveguide integrated on a Si chip. For example, a strip could be formed by etching a layered structure on Si, where those layers would be formed by successive epitaxial growth of Ge, GeSn, and Ge on the chip. Using doping at some epitaxy steps, a *p-i-n* diode strip could be formed whose cross-section is, for example 1.0 μm in width and 0.5 μm in height. The resulting waveguided EA modulators (or several such modulators) could be seamlessly or monolithically integrated with a variety of “cooperating” on-chip photonic components to form a photonic integrated circuit (PIC) or more generally an EPIC. Because the response of the present EA modulation begins at 1.9 μm and extends to longer wavelengths, it is ideal for 1.8 – 5.0 μm MIR applications.

Methods

Sample growth. The samples used in this study were grown on *p*-type double-side polished Si(001) substrates using molecular beam epitaxy at a base pressure of less than 2×10^{-10} torr. The first step of the epitaxy process was the growth of a strain-relaxed Ge virtual substrate (VS) using a two-step growth technique, including two 100 nm thick Si layers grown at 650 °C and 350 °C, a 60 nm thick Ge seed layer grown at 350 °C, followed by *in-situ* annealing at 800 °C for 5 min, and a 60 nm thick Ge buffer layer grown at 550 °C. Then, a B-doped *p*-type Ge layer was grown at 550 °C. The growth temperature was subsequently decreased to 150 °C for the growth of a GeSn active layer, followed by the growth of a Sb-doped *n*-type Ge layer. The epitaxial growth was completed with the growth of a 3 nm thick Si cap layer. The nominal doping in the *n*- and *p*-Ge layers is $5 \times 10^{18} \text{ cm}^{-3}$.

Device fabrication. The grown samples were fabricated into *p-i-n* diodes using CMOS-compatible processing technology. Circular mesas with different diameters in the 250 – 1000 μm range were created using standard optical lithography and reactive ion etching techniques. A SiO_2 passivation layer with a thickness of 400 nm was then deposited using an e-beam evaporator. Contact windows were then opened by wet etching using buffered oxide etchant (BOE) which provides high etching selectivity between Ge and SiO_2 . Ring-shaped Cr/Au bilayer metal pads with a thickness of 20/200 nm were deposited using an e-beam evaporator and patterned using lift-off techniques.

Transmission experiments. The transmission experiments were carried out at room temperature using a broadband quartz-tungsten-halogen (QTH) lamp as the light source. The light was filtered using a 1200 nm high-pass filter and dispersed using a monochromator equipped with a 600 line/mm grating blazed at 1600 nm. The dispersed light was then reshaped using an adjustable aperture and focused onto the top surface of the device using a 20 \times objective; this process ensured that the beam size was smaller than the window of the device. A square-wave AC bias with a frequency of 1 KHz was applied to the devices using an arbitrary wavefunction generator (Fluke, 282). The light transmitted through the device was then sent to a LN_2 -cooled InSb photodetector (1–5 μm detection range) and converted to an electrical signal, which was read out using a lock-in amplifier (Stanford Research System, SR830) to determine the

transmittance. The electric field applied to the GeSn active layer was estimated from the applied voltage (V) using $F = F_0 + V/t$, where F_0 is the built-in electric field in the $p-i-n$ junction.

AC experiments. The AC experiments were carried out at room temperature using a 2 μm laser (Thorlabs, LFL2000) as the light source. The laser was focused onto the top surface of the device using a 20 \times objective. The transmitted light through the device was then sent to an extended InGaAs photodetector (Thorlabs, DET10D2) with a photodetection cutoff wavelength of 2600 nm and a 3 dB bandwidth of 14.5 MHz. The electrical signal from the photodetector was then preamplified (Standard Research System, SR 560) and monitored using an oscilloscope (Tektronix, MSO 2000B).

For the 3-dB bandwidth experiments, we evaluated the 3-dB bandwidth at a 2000 nm wavelength. A 2000 nm laser (Thorlabs, LFL2000) was used as the light source. A vector network analyzer (Anritsu MS4647B) with a bias tee to combine DC bias and high-speed RF signals was used to generate the RF signals fed into the GeSn devices. The intensity of the transmitted light was then detected using a high-speed amplified extended InGaAs photodetector (Electro-Optics Technology, ET-5000A) with a rated bandwidth of >12.5 GHz and the signal was sent to the vector network analyzer S21 parameter (the ratio between the modulated optical signals and the RF signal) measurements.

Data availability. The data that support this work are available from the corresponding author upon request.

References

1. R. A. Soref, Silicon-based optoelectronics, *Proc. IEEE*. 81(12), 1687-1706 (1993).
2. R. Soref, The past, present, and future of silicon photonics. *IEEE J. Sel. Top. Quant. Electron.* **12**, 1678-1687 (2006).
3. R. Won, Integrating silicon photonics. *Nat. Photon.* **4**, 498-499 (2010).
4. C. Sun, M. T. Wade, Y. Lee, J. S. Orcutt, L. Alloatti, M. S. Georgas, A. S. Waterman, J. M. Shainline, R. R. Avizienis, S. Lin, B. R. Moss, R. Kumar, F. Pavanello, A. H. Atabaki, H. M. Cook, A. J. Ou, J. C. Leu, Y.-H. Chen, K. Asanović, R. J. Ram, M. A. Popović, V. M.

- Stojanović, Single-chip microprocessor that communicates directly using light. *Nature* **528**, 534-538 (2015).
5. D. Geuzebroek, R. Dekker, E. Klein, J. van Kerkhof, Photonic integrated circuits for visible light and near infrared: Controlling transport and properties of light, *Sensor. Actuat B-Chem.* **223**, 952-956 (2016).
 6. R. Soref, Mid-infrared photonics. In *Optical Fiber Communication Conference*, OSA Technical Digest (online); Optical Society of America, 2015, paper W4A.4.
 7. J. Liu, D. D. Cannon, K. Wada, Y. Ishikawa, S. Jongthammanurak, D. T. Danielson, J. Michel, L. C. Kimerling, Mid-infrared photonics in silicon and germanium. *Nat. Photon.* **4**, 495-497 (2010).
 8. T. Hu, B. Dong, X. Luo, T. Y. Liow, J. Song, C. Lee, G. Q. Lo, Silicon photonic platforms for mid-infrared applications. *Photon. Res.* **5**, 417-430 (2017).
 9. T. F. Refaat, S. Ismail, G. J. Koch, M. Rubio, T. L. Mack, A. Notari, J. E. Collins, J. Lewis, R. D. Young, Y. Choi, M. N. Abedin, U. N. Singh, Backscatter 2- μm Lidar validation for atmospheric CO₂ differential absorption Lidar applications. *IEEE Trans. Geosci. Remote Sensing* **49**, 572-580 (2011).
 10. M. Nedeljkovic, A. Z. Khokhar, Y. Hu, X. Chen, J. S. Penades, S. Stankovic, H. M. H. Chong, D. J. Thomson, F. Y. Gardes, G. T. Reed, G. Z. Mashanovich, Silicon photonic devices and platforms for the mid-infrared. *Opt. Mater. Express* **3**, 1205-1214 (2013).
 11. S. Wirths, R. Geiger, N. von den Driesch, G. Mussler, T. Stoica, S. Mantl, Z. Ikonik, M. Luysberg, S. Chiusi, J. M. Hartmann, H. Sigg, J. Faist, D. Buca, D. Grutzmacher, Lasing in direct-bandgap GeSn alloy. *Nat. Photon.* **9**, 88-92 (2015).
 12. J. Margetis, S. Al-Kabi, W. Du, W. Dou, Y. Zhou, T. Pham, P. Grant, S. Ghetmiri, A. Mosleh, B. Li, J. Liu, G. Sun, R. Soref, J. Tolle, M. Mortazavi, S. Q. Yu, Si-Based GeSn lasers with wavelength coverage of 2-3 μm and operating temperatures up to 180 K. *ACS Photon.* **5**, 827-833 (2015).
 13. J. Chrétien, N. Pauc, F. A. Pilon, M. Bertrand, Q. M. Thai, L. Casiez, N. Bernier, H. Dansas, P. Gergaud, E. Delamadeleine, R. Khazaka, H. Sigg, J. Faist, A. Chelnokov, V. Reboud, J. M. Hartmann, V. Calvo, GeSn lasers covering a wide wavelength range thanks to uniaxial tensile strain *ACS Photon.* **6**, 2462-2469 (2019).
 14. M. Oehme, L. Werner, M. Gollhofer, M. Schmid, M. Kaschel, E. Kasper, J. Schulze, Room-temperature electroluminescence from GeSn light-emitting pin diodes on Si. *IEEE Photon. Technol. Lett.* **23**, 1751-1753 (2011).
 15. H. H. Tseng, K. Y. Wu, H. Li, V. Mashanov, H. H. Cheng, G. Sun, R. A. Soref, Mid-infrared electroluminescence from a Ge/Ge_{0.922}Sn_{0.078}/Ge double heterostructure p-i-n diode on a Si substrate. *Appl. Phys. Lett.* **102**, 182106 (2013).
 16. B. J. Huang, C. Y. Chang, Y. D. Hsieh, R. A. Soref, G. Sun, H. H. Cheng, G. E. Chang, Electrically injected GeSn vertical-cavity surface emitters on silicon-on-insulator platforms *ACS Photon.* **6**, 1931-1938 (2019).

17. C Chang, H. Li, C. T. Ku, S. G. Yang, H. H. Cheng, J. Hendrickson, R. A. Soref, G. Sun, Ge_{0.975}Sn_{0.025} 320 × 256 imager chip for 1.6–1.9 μm infrared vision. *Appl. Opt.* **55**, 10170 (2016).
18. B. J. Huang, J. H. Lin, H. H. Cheng, G. E. Chang, GeSn resonant-cavity-enhanced photodetectors on silicon-on-insulator platforms. *Opt. Lett.* **43**, 1215-1218 (2018).
19. H. Tran, T. Pham, W. Du, Y. Zhang, P. Grant, J. Grant, G. Sun, R. Soref, J. Margetis, J. Tolle, B. Li, M. Mortazavi, S. Q. Yu, High performance Ge_{0.89}Sn_{0.11} photodiodes for low-cost shortwave infrared imaging. *J. Appl. Phys.* **124**, 013101 (2018).
20. J. J. Ackert, D. J. Thomson, L. Shen, A. C. Peacock, P. E. Jessop, G. T. Reed, G. Z. Mashanovich, A. P. Knights, High-speed detection at two micrometres with monolithic silicon photodiodes. *Nat. Photon.* **9**, 393-396 (2015).
21. G. T. Reed, G. Masganovich, F. Y. Gardes, D. J. Thomson, Silicon optical modulators. *Nat. Photon.* **4**, 518-526 (2010).
22. S. L. Chuang, *Physics of Photonic Devices*; Wiley: New York, 2009.
23. J. Liu, M. Beals, A. Pomerene, S. Bernardis, R. Sun, J. Cheng, L. C. Kimerling, J. Michel, Waveguide-integrated, ultralow-energy GeSi electro-absorption modulators. *Nat. Photon.* **2**, 433-437 (2008).
24. R. A. Soref, G. Sun, H. H. Cheng, Franz-Keldysh electro-absorption modulation in germanium-tin alloys. *J. Appl. Phys.* **111**, 123113 (2012).
25. M. Oehme, K. Kosteki, M. Schmid, M. Kaschel, M. Gollhofer, K. Ye, D. Widmann, R. Koerner, S. Bechler, E. Kasper, J. Schulze, Franz-Keldysh effect in GeSn pin photodetectors. *Appl. Phys. Lett.* **104**, 161115 (2014).
26. D. Feng, S. Liao, H. Liang, J. Fong, B. Bijlani, R. Shafiiha, B. J. Luff, Y. Luo, J. Cunningham, A. V. Krishnamoorthy, M. Asghari, High speed GeSi electro-absorption modulator at 1550 nm wavelength on SOI waveguide. *Opt. Express* **20**, 22224-22232 (2012).
27. L. Mastronardi, M. Banakar, A. Khokhar, N. Hattasan, T. Rutirawut, T. D. Bucio, K. M. Grabska, C. Littlejohns, A. Bazin, G. Mashanovich, F. Gardes, High-speed Si/GeSi heterostructure electro absorption modulator. *Opt. Express* **26**, 6663-6673 (2018).
28. Y. H. Kuo, Y. K. Lee, Y. Ge, S. Ren, J. E. Roth, T. I. Kamins, D. A. B. Miller, J. S. Harris, Strong quantum-confined Stark effect in germanium quantum-well structures on silicon. *Nature* **437**, 1334-1336 (2005).
29. P. Chaisakul, D. Marris-Morini, M. S. Rouifed, G. Isella, D. Chrastina, J. Frigerio, X. L. Roux, S. Edmond, J. R. Coudeville, L. Vivien, 23 GHz Ge/SiGe multiple quantum well electro-absorption modulator. *Opt. Express* **20**, 3219-3224 (2012).
30. M. A. V. Camp, S. Assefa, D. M. Gill, T. Barwicz, S. M. Shank, P. M. Rice, T. Topuria, W. M. J. Green, Demonstration of electrooptic modulation at 2165 nm using a silicon Mach-Zehnder interferometer. *Opt. Express* **20**, 28009-28016 (2012).
31. W. Cao, D. Hagan, D. J. Thomson, M. Nedeljkovic, C. G. Littlejohns, A. Knights, S. Alam, J. Wang, F. Gardes, W. Zhang, S. Liu, K. Li, M. S. Rouifed, G. Xin, W. Wang, H. Wang,

- G. T. Reed, G. Z. Mashanovich, High-speed silicon modulators for the 2 μm wavelength band. *Optica* **5**,1055-1062 (2018)
32. M. Montesinos-Ballester, V. Vakarın, J. M. Ramirez, Q. Liu, C. Alonso-Ramos, X. L. Roux, J. Frigerio, A. Ballabio, A. Barzaghi, L. Deniel, D Bouville, L. Vivien, G. Isella, D. Marris-Morini, Optical modulation in Ge-rich SiGe waveguides in the mid-infrared wavelength range up to 11 μm . *Communications Materials* **1**, 6 (2020)
 33. S. Bao, G. Y. Chong, Y. H. Tan, E. A. Fitzgerald, and C. S. Tan, Defects reduction of Ge epitaxial film in a germanium-on-insulator wafer by annealing in oxygen ambient. *APL Mater.* **3**, 016102 (2015).
 34. Q. Zheng, L. Xia, L. Tang, C. Du, H. Cui, Low Voltage Graphene-Based Amplitude Modulator for High Efficiency Terahertz Modulation. *Nanomaterials*. **10**, 585 (2020).
 35. S. Jongthammanurak, J. Liu, K. Wada, D. D. Cannon, D. T. Danielson, D. Pan, L. C. Kimerling, J. Michel, Large electro-optic effect in tensile strained Ge-on-Si films. *Appl. Phys. Lett.* **89**, 161115 (2006).
 36. J. I. Pankove, *Optical Processes in Semiconductors*; Dover Publications: New York, 1971.
 37. Y. Hinakura, Y. Terada, T. Tamura, T. Baba, Wide spectral characteristics of Si photonic crystal mach-zehnder modulator fabricated by complementary metal-oxide-semiconductor process. *Photon.* **3**, 17 (2016).
 38. G. E. Chang, R. Basu, B. Mukhopadhyay, P. K. Basu, Design and modeling of GeSn-based heterojunction phototransistors for communication applications. *IEEE J. Sel. Top. Quant. Electron.* **22**, 425-433 (2016).
 39. G. E. Chang, S. W. Chang, S. L. Chuang, Strain-balanced $\text{Ge}_z\text{Sn}_{1-z}\text{-Si}_x\text{Ge}_y\text{Sn}_{1-x-y}$ multiple-quantum-well lasers. *IEEE J. Quantum Electron.* **46**, 1813-1820 (2010).

Acknowledgments

This work at National Chung Cheng University was supported by the Ministry of Science and Technology, Taiwan (MOST) under project numbers: MOST 106-2628-E-194-003-MY2, MOST 108-2221-E-194-055, and MOST 109-2636-E-194-002. We thank Dr. Hui Li, who is formerly from National Taiwan University, Taiwan, and Mr. Kuan-Chih Lin and Mr. Chih-Yuan Cheng, who are from National Chung Cheng University, Taiwan, for their assistance in the experiments. We also thank the Taiwan Semiconductor Research Institute (TSRI), Taiwan for assistance in high-speed experiments.

Author contributions

G. E. Chang conceived the initial idea of this work and designed the devices. H. H. Cheng designed and prepared the materials used in this study and carried out material characterizations. Y. D. Hsieh and J. H. Lin fabricated and characterized the devices. G. E. Chang performed the theoretical simulations. G. E. Chang, H. H. Cheng, R. A. Soref, and G. Sun performed the data analysis and prepared the manuscript. G. E. Chang supervised the entire project.

Additional Information

Supporting Information accompanying this paper is available.

Competing interests: The authors declare no competing financial interests.

Figures

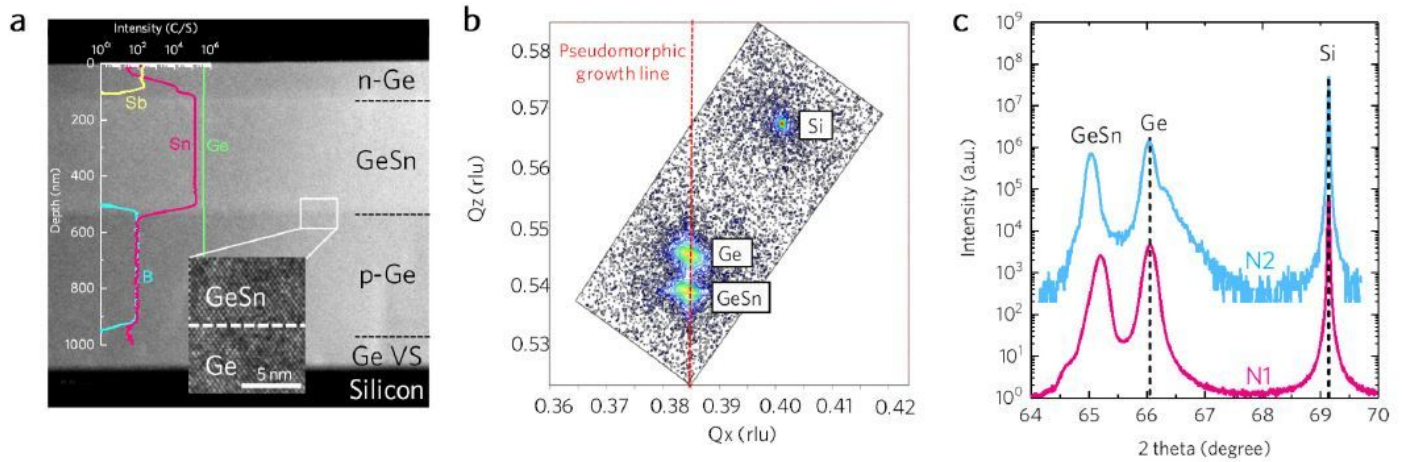


Figure 1

Material characterization of the grown samples. (a) Cross-sectional transmission electron microscopy (XTEM) image of sample N1 overlapped with secondary ion mass spectrometry (SIMS) atomic distribution. The inset shows a high-resolution XTEM image of the Ge/GeSn interface, revealing pseudomorphic growth. (b) (224) reciprocal-space mapping (RSM) of sample N1, showing pseudomorphic GeSn/Ge heterostructures. (c) ω - 2θ scan of the samples, showing shifted GeSn peaks with increasing Sn composition.

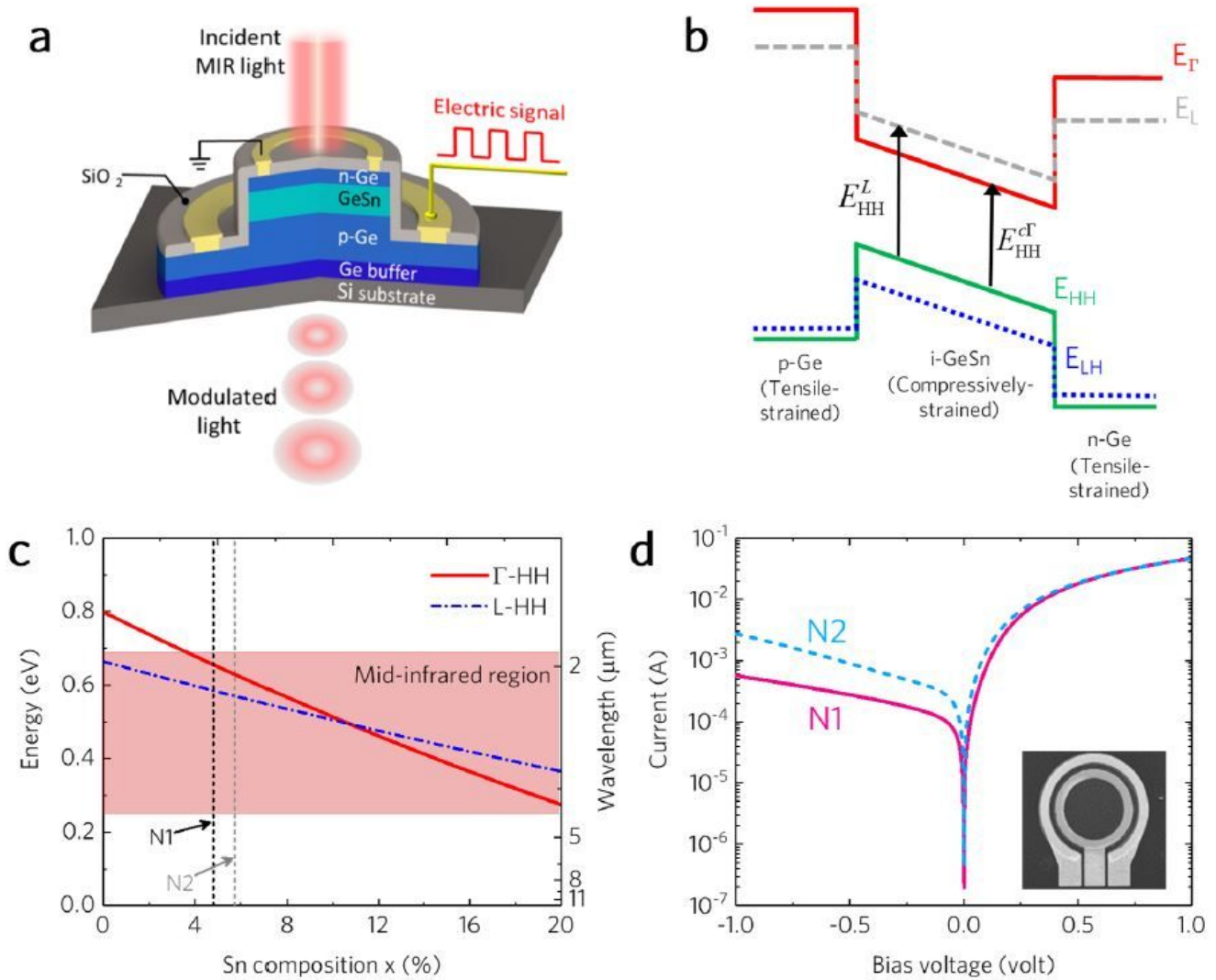


Figure 2

GeSn p-i-n diodes on silicon for MIR EA modulation. (a) Schematic of our designed normal-incident GeSn p-i-n diode on (001) silicon for optical modulation (not to scale). The mid-infrared (MIR) light beam is incident on the top of the device and transmitted through the GeSn active layer. AC bias voltage is applied to the p-i-n diode to modulate the MIR light based on the FK effect. (b) Schematic band diagram of Ge/GeSn/Ge heterojunction with an applied electric field. The compressive strain in the GeSn active layer splits the valence band. (c) Evolution of the lowest direct-gap transition energy (from the heavy-hole (HH) to L-conduction band) and indirect-gap transition energy (HH to L-conduction band) for pseudomorphic GeSn on Ge at 300 K as a function of Sn composition calculated using deformation potential theory. The epitaxially grown GeSn heterostructure samples N1 and N2 are indicated by the dashed lines. (d) Current-voltage characteristics of the fabricated GeSn p-i-n diodes with $D=250\ \mu\text{m}$. The inset shows top-view scanning electron microscopy (SEM) image of the fabricated diode.

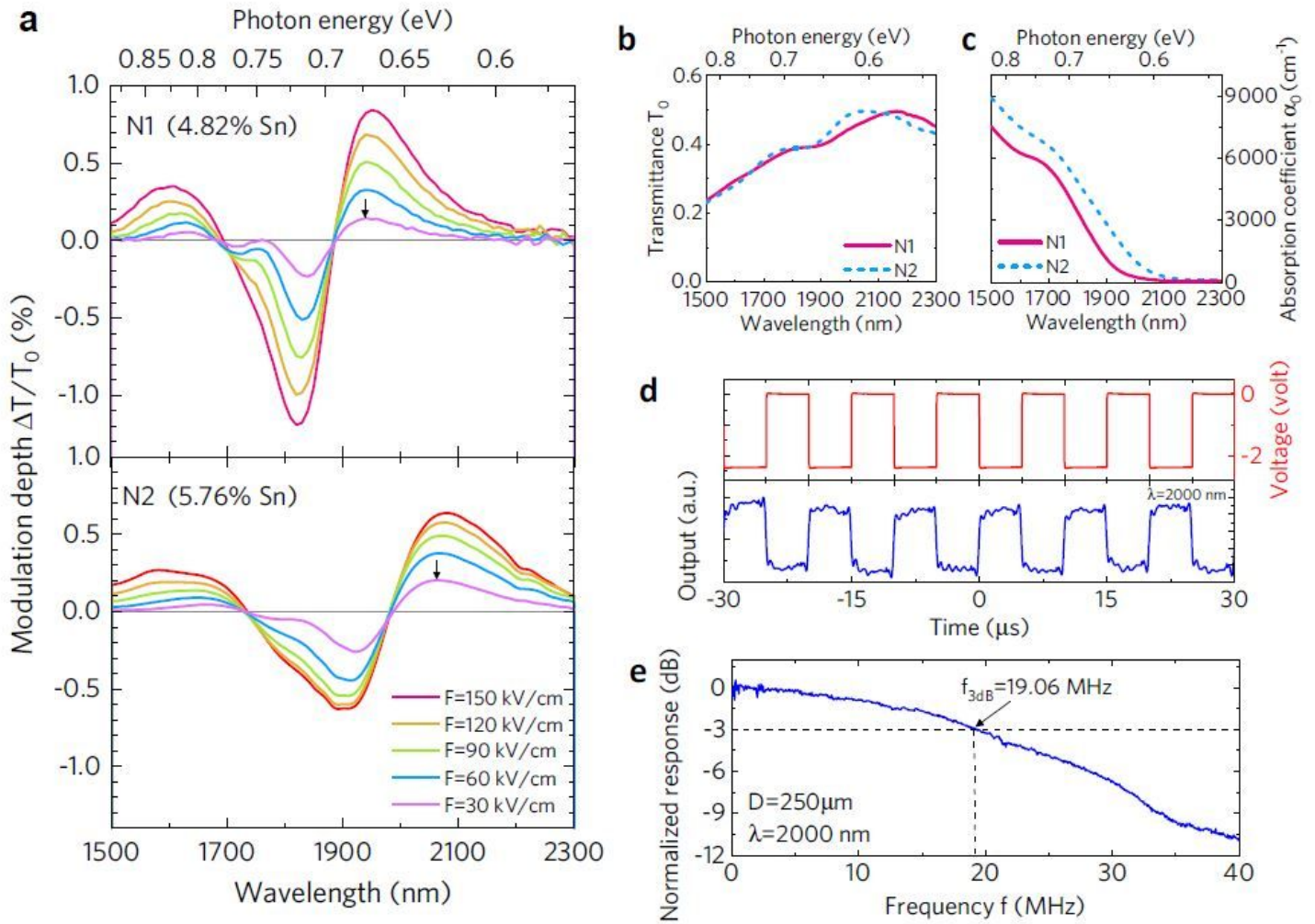


Figure 3

Modulation characteristics at room temperature: (a) Modulation depth spectra of the GeSn devices measured at different applied electric fields. Clear variations in transmittance are observed, providing strong evidence of the FK effect. The lowest direct transition energies are indicated by the solid arrows. (b) Transmittance spectra for the GeSn devices and (c) absorption spectra under zero bias conditions for the GeSn active layers. (d) AC optical modulation at 100 kHz at 2000 nm wavelength for device N1. (e) Normalized radio frequency response of device N1 ($D=250\ \mu\text{m}$) at 2000 nm showing a 3 dB bandwidth of 19.06 MHz.

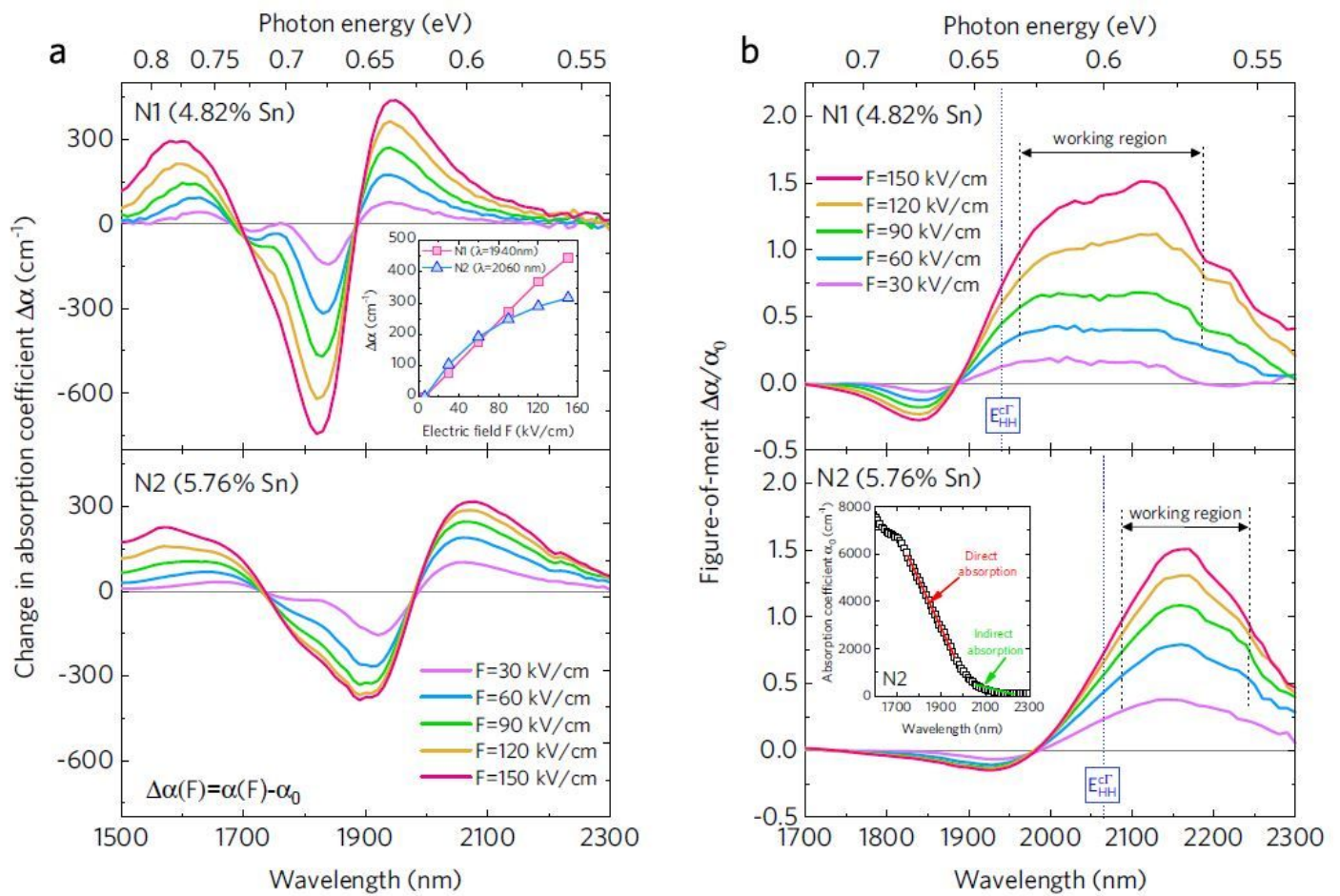


Figure 4

Franz-Keldysh effect in GeSn. (a) Change in the absorption coefficient in the GeSn active layers at different applied electric fields. The inset shows the change in the absorption coefficient for device N1 and device N2 at $\lambda=1940$ and $\lambda=2060$ nm, respectively, as a function of electric field. (b) Figure-of-merit (FOM) $\Delta\alpha/\alpha_0$ for the GeSn active layer at different applied electric fields. The lowest direct bandgap is indicated by the dashed blue lines. The inset shows the absorption coefficient spectrum under the zero-bias condition of device N2.

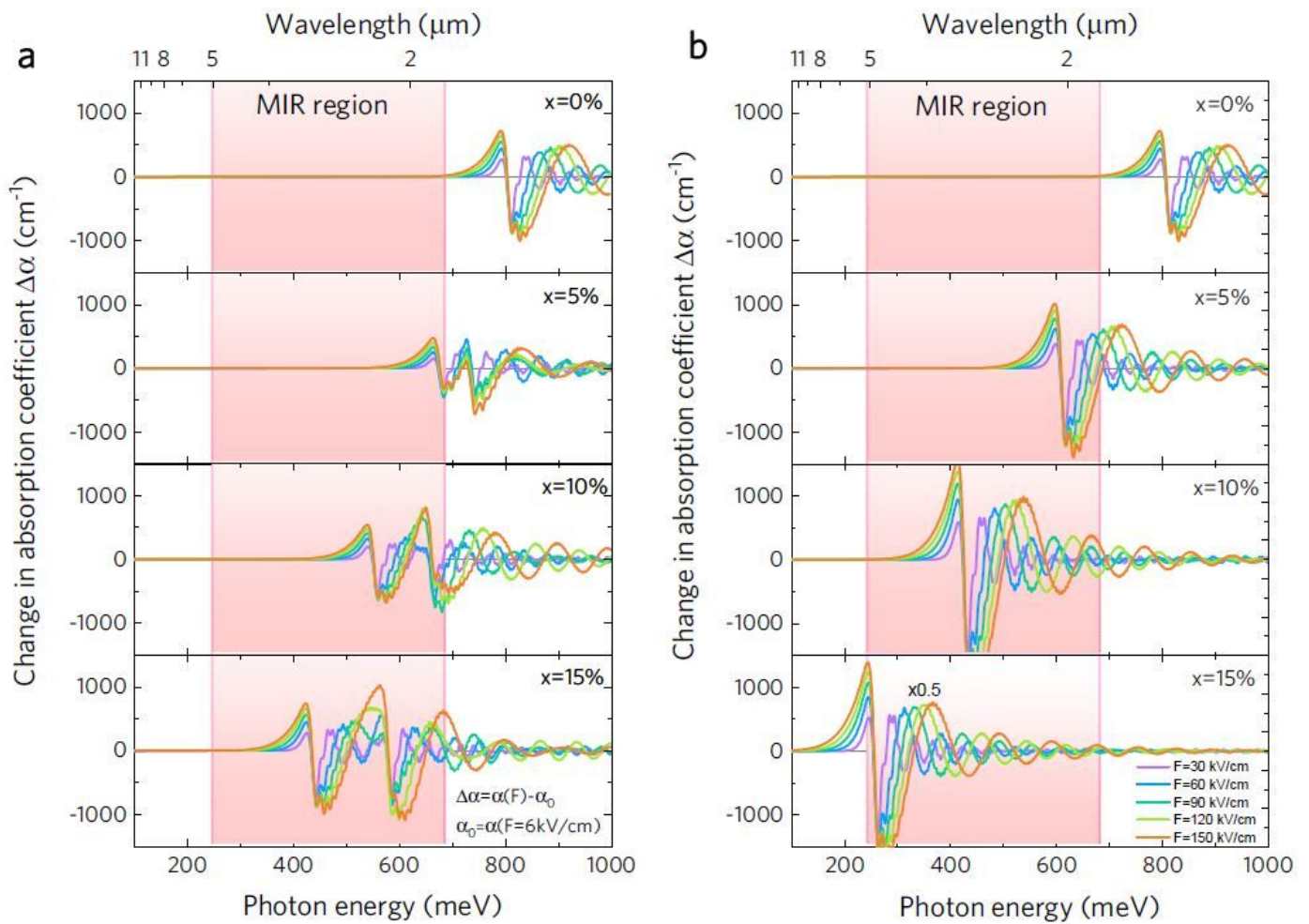


Figure 5

Theoretical modeling for Franz-Keldysh effect in GeSn. Calculated change-in-absorption coefficient $\Delta\alpha$ at $T=300$ K for (a) pseudomorphic $\text{Ge}_{1-x}\text{Sn}_x$ on Ge and (b) unstrained $\text{Ge}_{1-x}\text{Sn}_x$ with different Sn contents and electric fields.

Supplementary Files

This is a list of supplementary files associated with this preprint. Click to download.

- [GeSneamcommV11supportingforeditingfinished.pdf](#)